

# IFU observations of the GRB 980425/SN 1998bw host galaxy: emission line ratios in GRB regions <sup>★</sup>

L. Christensen<sup>1</sup>, P. M. Vreeswijk<sup>2</sup>, J. Sollerman<sup>2,3</sup>, C. C. Thöne<sup>2</sup>, E. Le Floc'h<sup>4</sup>, and K. Wiersema<sup>5</sup>

<sup>1</sup> European Southern Observatory, Casilla 19001, Santiago 19, Chile, e-mail: lichrist@eso.org

<sup>2</sup> Dark Cosmology Centre, Niels Bohr Institute, University of Copenhagen, Juliane Maries Vej 30, 2100 Ø, Denmark

<sup>3</sup> Department of Astronomy, AlbaNova, 106 91, Stockholm University, Sweden

<sup>4</sup> Spitzer Fellow, Institute for Astronomy, 2680 Woodlawn Drive, Honolulu HI 96822, USA

<sup>5</sup> University of Leicester, University Road, Leicester, LE1 7RH, United Kingdom

Received 3 April 2008/Accepted 16 July 2008

## ABSTRACT

**Context.** The collapsar model predicts that the progenitors of Gamma-ray Bursts (GRBs) are metal poor in Fe group elements. The existence of low metallicity stellar populations could manifest itself through special characteristics of the immediate environment of the GRB site in the host galaxy.

**Aims.** We analyse the strong emission lines from the sub-luminous host galaxy of GRB 980425, which showed the first connection with a supernova explosion (SN 1998bw). The host has a sufficient size to allow detailed resolved spectroscopy of individual H II regions and to look for regions with special properties close to the GRB site.

**Methods.** Using integral field spectroscopy with VIMOS we cover most of the high surface brightness part of the host including the H II region where the supernova and GRB occurred.

**Results.** The star formation rate, reddening, equivalent width and stellar mass in the GRB region is similar to other H II regions in the host. Extreme values arise in the only region that shows emission lines from Wolf-Rayet stars; a region that lies 800 pc in projection from the GRB site. Strong emission line diagnostics of all H II regions imply oxygen abundances between 0.3 and 0.8 solar with the lowest values arising in the WR and GRB regions, although including uncertainties from the metallicity diagnostics, all metallicities are similar within  $3\sigma$ . We show a good agreement between the luminosity weighted and mass weighted specific star formation rates (SSFR) in individual young H II regions. While the global average of the SSFR is similar to high redshift GRB hosts, there are significant variations between individual resolved H II regions. Comparing the measured emission line ratios for a sample of low redshift GRB hosts to theoretical models and to observations of field galaxies, we find that GRBs arise in a range of metallicity environments while the regions are consistently very young. The similar line ratios of GRB hosts compared to the WR region can arise in spatially unresolved galaxies with bright H II regions near the GRB location.

**Key words.** Galaxies: abundances – Galaxies: individual – Gamma rays: bursts

## 1. Introduction

The association of the Gamma-Ray burst GRB 980425 and the supernova SN 1998bw (Galama et al. 1998) was initially questioned due to the very low redshift of the supernova host galaxy ESO 184-G82,  $z = 0.0085$ . The corresponding isotropic energy output for GRB 980425 was very low ( $E \sim 10^{49}$  erg) compared to other GRBs known at that time (at  $z \gtrsim 1$  with  $E \sim 10^{52}$  erg). Since then, more apparently under-luminous, low redshift GRB events have been detected. The definite proof of a supernova connection came with the discovery of SN Type Ic signatures in the afterglow spectra of a couple of long duration GRBs (Hjorth et al. 2003; Stanek et al. 2003; Malesani et al. 2004). While the energetics of GRB 980425 suggested an underluminous event, there is no indication that the supernova that accompanied it was peculiar for a GRB-SN (Kaneke et al. 2007).

Throughout the past 10 years, around 500 GRBs have been observed with optical afterglows detected for about a third of these<sup>1</sup>. While the bursts sampled by the BeppoSAX satel-

lite typically had redshifts  $z \sim 1$ , the ones detected by the Swift satellite (Gehrels et al. 2004) have an average redshift of 2.2 (Jakobsson et al. 2006)<sup>2</sup>. The small angular size of the high redshift host galaxies (typically less than a few arcseconds) implies that a closer examination of the nature of the hosts must come from integrated spectra or even broad band images for the faintest of the hosts. Images of GRB hosts show that the GRBs are preferentially located in sub-luminous (Le Floc'h et al. 2003) actively star forming, young galaxies (Christensen et al. 2004a). The distribution of the GRB afterglow locations within their hosts generally follow the bright continuum light distribution in the host galaxies (Bloom et al. 2002; Fruchter et al. 2006).

Models of single star collapsar progenitors for the long duration bursts predict a preference for metal poor environments (Woosley 1993). Generally, low metallicities of the surrounding medium of GRBs are inferred from absorption line studies of GRB afterglows at  $z \gtrsim 2$  (Savaglio et al. 2003; Vreeswijk et al. 2004; Chen et al. 2005; Dessauges-Zavadsky et al. 2006; Prochaska et al. 2007). This technique is mostly used to infer iron group elements in the line

<sup>★</sup> Based on observations collected at the European Southern Observatory, Chile: programme ID 077.D-0488(A), and archive programmes: 64.H-0375(A), 66.D-0576(A) and 275.D-5039(A).

<sup>1</sup> <http://www.mpe.mpg.de/~jcg/grbgen.html>

<sup>2</sup> <http://www.astro.ku.dk/~pallja/GRBsample.html>

of sight towards the GRB. High resolution spectra of GRB afterglows have indicated that the medium which is probed lies at distances greater than several tens of pc from the burst site (Prochaska et al. 2006; Chen et al. 2007), and a detailed study for one burst (GRB 060418) shows that the environment probed by the absorption lines lies at a distance of 1.7 kpc from the burst site (Vreeswijk et al. 2007). Thus the GRB afterglow does not probe the immediate surrounding medium of the burst itself, but rather the interstellar medium of the host and this implies that we may not be able to estimate directly the metallicity of the progenitor using this technique.

Since the hosts of long duration bursts are undoubtedly star forming galaxies, their emission lines can be used to infer the metallicities from the integrated optical spectra, provided that the redshift of the GRB is less than  $\sim 1$  for which the strong lines are visible in the optical. This technique is generally used to derive the oxygen abundance. Diagnostics of strong emission lines for the hosts of GRB 980425, GRB 020912, GRB 030329, GRB 031203, and GRB 060218 have indicated sub solar metallicities (Prochaska et al. 2004; Hammer et al. 2006; Gorosabel et al. 2005; Sollerman et al. 2005; Wiersema et al. 2007), and systematically lower host galaxy metallicities than found in nearby ordinary Type Ic supernovae sites (Modjaz et al. 2008). It is, however, not clear how the observed integrated GRB host spectra relate to the overall properties of the hosts, or to the very site where the GRB exploded. In a few cases where the host galaxy is clearly extended, the analysis of the spatially resolved emission lines can reveal what is special about the exact GRB region, or alternatively what specific environments are needed to make a GRB. Thöne et al. (2008) investigated the spectra of the host of GRB 060505, and found the GRB site to be the youngest and most metal poor area among the regions probed by the slit spectrum.

In the case of the host of GRB 980425/SN 1998bw (ESO 184-G82), which is a dwarf SBc galaxy, the SN occurred in a star forming region in the spiral arm. The region was identified through high spatial resolution images using HST/STIS (Fynbo et al. 2000) and confirmed by the observation of a fading source in this region (Sollerman et al. 2002). The location of the SN was offset by a projected distance of 0.8 kpc from the strongest star forming region in the host, that has distinct spectral signatures from Wolf-Rayet stars (Hammer et al. 2006). The spectrum of the SN region does not show any detected WR features. Other GRB hosts at  $z \lesssim 0.1$  do not show clear signatures of WR stars in emission either (Margutti et al. 2007; Wiersema et al. 2007). At higher redshifts, the absence of C iv  $\lambda$  1550 absorption lines from winds from WR stars can be explained by the afterglow which ionises the surrounding medium to a large radius (Chen et al. 2007, but see also Starling et al. (2005)).

All the hitherto performed analyses of the emission lines from GRB hosts are limited to the region within the slit. Hence the data can be affected by slit-losses leading to under-estimation of the integrated star formation rate (SFR). In this paper, we present data for the GRB 980425 host galaxy obtained with integral field spectroscopy. The data from the VIMOS integral field unit (IFU) presented in Sect. 2 allow us to cover a large fraction of the surface of the host with a resolution of 0.27 kpc, and to analyse most of the high surface brightness regions (see Fig. 1). We use the data to make maps of emission lines and their ratios to determine the reddening, SFRs, specific SFRs, metallicities, densities, temperatures, kinematic and stellar masses, as presented in Sect. 3. We compare the emission line ratios to those of other GRB hosts in Sect. 4, and show evidence that

while the abundances may vary, the regions are very young in all cases. In Sect. 5 we discuss the implications for the unresolved high redshift GRB hosts. We adopt a cosmology with  $H_0 = 70 \text{ km s}^{-1} \text{ Mpc}^{-1}$  throughout the paper.

## 2. Observations and data reduction

The host galaxy was observed on six different clear or photometric nights in April and May 2006 in service mode at the Very Large Telescope UT3 *Melipal* with the VIMOS integral field spectroscopic mode. The high spectral resolution setup of VIMOS consists of four quadrants of 400 spectra each, recorded on 4 CCDs. The field of view (FOV) when using the 0'.67 lens array is  $27'' \times 27''$ . The size of the host as measured in FORS images obtained from the ESO archive (64.H-0375 and 66.D-0576(A), PI: F. Patat), is about 1' in diameter, while the high surface brightness emission is roughly half that size. We obtained a total integration time of five hours in three different settings as listed in Table 1. Since the host galaxy emission occupies the whole IFU FOV (see Fig. 1), separate 200 s observations of the sky offset by 2 arcmin were used for sky background subtraction. The wavelength coverage of the VIMOS data from the three settings allowed us to cover all of the strong emission lines used for abundance determinations. The low spectral resolution data also cover the [O II]  $\lambda$ 3727 line. At the redshift of the host this emission line falls at 3759 Å, where the transmission of the VIMOS IFU is around 10 times lower than at maximum.

The data were reduced with the reduction package P3d (Becker 2002) and the following steps. After bias subtraction, the location of the 1600 spectra and the traces were found using continuum lamp spectra obtained immediately after the science observations. Arc line spectra taken after science exposures were extracted. The science spectra were extracted, wavelength calibrated and flat fielded using the (wavelength dependent) transmission function determined from the continuum spectra. The calibrated science data were arranged in a 3D data cube. Each data cube was corrected for the atmospheric extinction. The sky background was subtracted using the separately reduced sky background data cubes.

The 4 quadrants in the combined data cubes were flux calibrated separately using observations of spectrophotometric stars placed in each of the four quadrants. Spatial shifts between the individual data cubes were determined and the cubes were combined, using routines similar to standard image combination procedures in IRAF, while masking out the dead spectra that are located mainly at the edge of the FOV. We ignored the differential atmospheric refraction effects, since the observations were mostly taken at air masses less than 1.4. This should theoretically cause a maximum shift of  $\sim 1$  spaxel (a spaxel 'spatial picture element' is defined as a single spectrum in the array) from the blue to the red end of the spectral range (Filippenko 1982). However, a maximum spatial shift in the data cubes was measured to be less than 0.2 pixels from cross correlation technique. Since we used dithered pointings that were offset by  $3''$ , the resulting FOV in the reduced and combined data cube is  $30'' \times 30''$ .

To check the absolute flux calibration we re-reduced broad band FORS *B*, *V*, and *R* images from the ESO archive. We then extracted the spectra for different regions from the VIMOS high spectral resolution cubes, and convolved with the Bessell filter transmission functions to calculate the broad band magnitudes (Bessell 1990). For individual regions, e.g. the SN and WR region and the whole VIMOS FOV in Fig. 1, the magnitudes and colours are in agreement with the FORS images to within 10% accuracy. It is not possible to apply a simple scaling

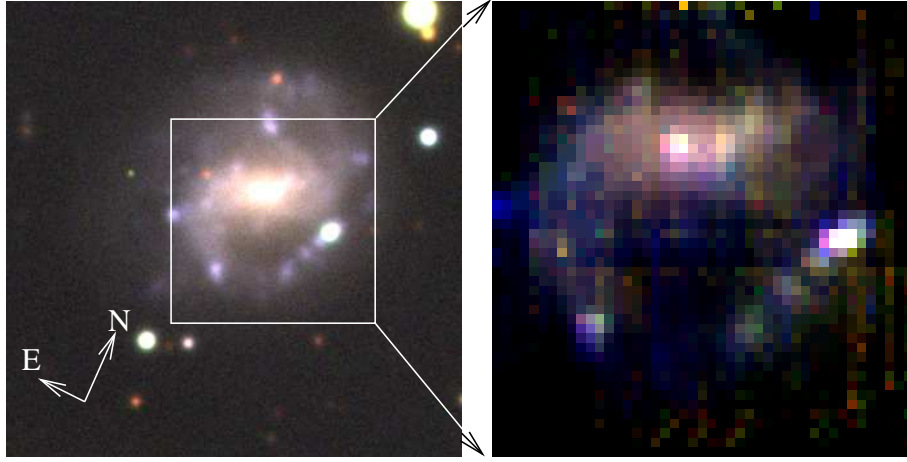


**Fig. 1.** Colour composite images of the host galaxy from archive FORS *BVR* broad band images (left) and broad band images extracted from the VIMOS data cube (right). Each of the pixels in the VIMOS image has a corresponding spectrum. The WR region is the brightest and bluest one to the West of the centre, and the SN region is seen as a fainter extension adjoining this region to the South. The size of the VIMOS image is  $30''$  on a side, corresponding to 5.3 kpc at the redshift of the galaxy. *See the electronic edition of the Journal for a colour version of this figure.*

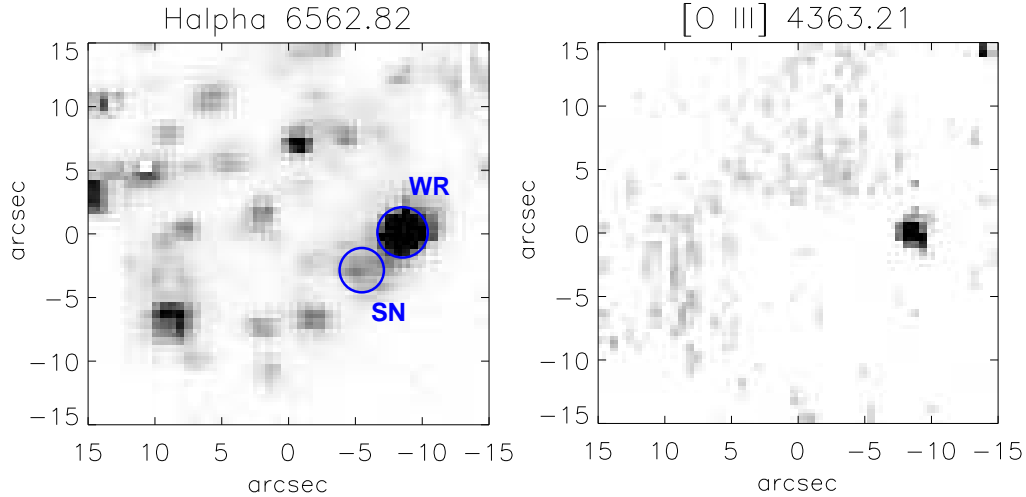


**Fig. 2.** Maps of a typical strong emission line (left:  $H\alpha$ ), and a faint one (right:  $[O\text{ III}] \lambda 4363$ ). The region that is bright in  $[O\text{ III}]$  is the only region where emission lines from WR stars are detected. The circles have a radius of  $2''.5$  corresponding to 440 pc.

to the VIMOS data cube to improve the absolute spectrophotometric calibration for all regions within the FOV. The sensitivity of the VIMOS-IFU is known to show variations depending on the exact location of the spectrophotometric standard star (see Monreal-Ibero et al. 2006), which affects the absolute flux calibration. Finally, the data cube was corrected for the foreground Galactic reddening of  $E_{B-V}=0.059$  mag (Schlegel et al. 1998).

Even though the VIMOS data were taken in good seeing conditions, using the  $0''.67$  spatial sampling gives an effective resolution element of  $1''.5$ , or 0.27 kpc at the redshift of the galaxy.

### 3. Results

#### 3.1. Emission line maps and spectra

IFU data cubes allow us to estimate fluxes both from images and from spectra. Two-dimensional images are created by co-adding monochromatic slices (equivalent to channel maps in the radio astronomy community) in the data cube along the wavelength di-

rection. These can be analysed with standard imaging methods. One-dimensional spectra are created by selecting some pixels or ‘spaxels’ in the data cube and co-adding each wavelength separately. To extract one dimensional spectra and visualize the data cubes we used the program QFitsView created by Thomas Ott.

To estimate line fluxes we used two methods: fitting the lines in the spectra with Gaussian profiles and a simple integration of narrow-band images created from the data cube. Since the emission lines from the different regions are not strictly Gaussian in shape, we can not rely on a fully automated line fitting routine to extract line fluxes. To create emission line maps and to derive fluxes for different regions, we use the second method, integrating over 8 slices from the data cube in the spectral direction centered on the measured wavelength  $(1+z)\lambda_{\text{lab}}$ . This corresponds to twice the spectral *FWHM* and is equivalent to integrating over a wavelength interval between 4.4 and 4.7 Å around the lines. The emission lines are barely resolved even with the high spectral resolution ( $\sim 110 \text{ km s}^{-1}$  at 5000 Å), and none of the emission lines in any of the regions have widths significantly higher than

Date	Integration time (s)	Setting	$\lambda$ (Å)	$R$ ( $\lambda/\Delta\lambda$ )	Seeing ( $''$ )
2006 April 25	3×600	LR blue	3600–6800	250	0.9
2006 May 24	2×600	LR blue	3600–6800	250	0.9
2006 April 29	3×1800	HR orange	5045–7475	2700	0.7
2006 May 3	2×1800	HR orange	5045–7475	2700	0.8
2006 May 24	2×1800	HR blue	3970–6230	2600	1.0
2006 May 25	1×1800	HR blue	3970–6230	2600	0.4

**Table 1.** Log of the observations.  $R$  gives the average spectral resolution as measured from the data. The resolution varies by 10% from one spectrum to the next. The seeing is the one recorded by the observatory DIMM monitor, and not the effective spatial resolution obtained from the data cube.

the spectral resolution. The emission line fluxes determined from the two methods are consistent to within 10% accuracy.

The continuum flux was determined by fitting a first order polynomial over a region around the emission line in each of the individual spectra. The continuum region was selected free of other emission lines, and was examined interactively. The backgrounds were subtracted to give the pure emission line maps. Two examples are presented in Fig. 2, which shows the  $H\alpha$  emission line map (left) and  $[O III] \lambda 4363$  (right). Only the brightest  $H II$  region in the host shows detectable emission from the latter, faint, temperature sensitive line. This region also shows emission lines with characteristic Wolf-Rayet features (Hammer et al. 2006). We investigated the emission line maps to look for WR emission lines (He or N lines) in other regions, but these lines lie below the detection limit in the data cube. Following Hammer et al. (2006) the brightest region is denoted ‘WR’, while the star forming region in which the SN/GRB occurred is denoted ‘SN’. The SN occurred in an  $H II$  region which lies 5 arcsec to the South-East of the centre of the WR region, or 800 pc in projection at the redshift of the host. In the spectrum extracted from the WR region we identify 45 different lines within the spectral coverage<sup>3</sup>. In other regions the number of detectable lines is significantly smaller. This paper mostly deals with strong emission lines, as these can be identified throughout the host galaxy, allowing for a fair comparison of different regions.

### 3.2. Emission line fluxes

Table 2 lists the line fluxes and derived properties for several distinct and spatially resolved  $H II$  regions identified in the  $H\alpha$  map. Most of the regions listed in the table are simply labeled with their coordinates relative to the  $H\alpha$  map. A large fraction (34%) of the integrated emission line flux within the VIMOS FOV comes from the WR region. The last row in the Table presents the sample mean and standard deviation as a measure of the spread of the values in the different  $H II$  regions.

The  $H\alpha$  and  $H\beta$  Balmer emission line fluxes have been corrected for an underlying stellar absorption component with the equivalent width  $EW(H\alpha) \approx EW(H\beta) = 2.6 \text{ Å}$  which is an appropriate value for young stellar populations (González Delgado et al. 1999). In none of the spaxels do we see evidence for an absorption line around the  $H\beta$  line. While the absorption line should be present in any stellar population, the non-detection in the individual spectra is due to the fact that the continuum emission is very faint, and the signal-to-noise ratio in each spaxel is typically only a few. In the combined galaxy

spectrum there is an indication of an underlying stellar absorption component with an equivalent width of  $\sim 2 \text{ Å}$ .

The equivalent width is defined as  $EW = \int_{\lambda} (f_{line,\lambda}/f_{cont,\lambda} - 1)d\lambda$ , where  $f_{line,\lambda}$  is the measured emission line flux and  $f_{cont,\lambda}$  is the continuum flux. We can correct the integrated line flux for an absorption of  $2.6 \text{ Å}$ :  $f_{line,cor} = f_{line} + 2.6 \times f_{cont}$ . For regions with fainter Balmer emission line fluxes, and equivalent widths the correction to the  $H\beta$  line can be as substantial as 15%. This implies that the extinction will be over-estimated, and the metallicity under-estimated if this correction is not applied. For the brightest emission line regions the corrections are small.

The  $[O II]$  emission line in the low spectral resolution data has a considerably larger uncertainty than the other bright emission lines. Furthermore, no spectrophotometric standard star was observed with the low spectral resolution setup at the dates of the observations. Instead we used standard star observations that differed by about one week in time, and relied on the fact that the overall shape of the transmission function of VIMOS is stable with time. To derive the emission line fluxes, we compared the extracted  $H\beta$  fluxes for the  $H II$  regions, and applied a scaling to the  $[O II]$  emission line.

If we are to compare the line fluxes of the WR and SN regions with those reported from long slit spectra in the literature (Sollerman et al. 2005; Hammer et al. 2006), as well as the FORS spectra obtained from the ESO archive (Program ID 275.D-5039(A), PI: Patat), we must take into account the different spatial sampling of the regions. Due to different effects such as seeing dependent slit losses, an uncertain placement of the slit, different spectral resolutions, seeing, as well as reduction procedures to extract the one dimensional spectra, it is difficult to compare directly our extracted fluxes with values in the literature (e.g. Sollerman et al. 2005; Hammer et al. 2006). As an example, the fluxes from the literature agree with our results obtained from the archive FORS long slit spectrum within a factor of  $\sim 2$  only. For these reasons we cannot compare the VIMOS spectra with those derived from long slit spectra. While slit losses affect the long slit spectra, the ratios of the emission line fluxes should remain the same as in the IFU data provided that the same region is extracted. The  $H\alpha/H\beta$  emission line ratio is frequently used to estimate the extinction (see Sect. 3.5), and in the SN region this ratio is used to infer both zero extinction (Sollerman et al. 2005) and  $A_V=1.02$  (Hammer et al. 2006), while we find  $A_V=1.95$  for  $R_V=3.1$  in the IFU data. Also for other emission line ratios of lines with similar wavelengths do we find differences of up to a factor of two. This could be due to spectrally blended lines, or blending of separate  $H II$  regions due to seeing.

The broad band magnitudes derived for these regions agree with the FORS imaging data to within 5–10%, which we take as representative for the uncertainty of the emission line fluxes.

<sup>3</sup> The spectrum presented in Hammer et al. (2006) also has significantly more lines than listed in the paper.

This uncertainty dominates relative to the pure statistical uncertainty derived from the number counts extracted for each line and region in the non-flux calibrated data ( $< 3\%$  for the faintest lines in Table 2). The uncertainties of the  $H\alpha$  and  $H\beta$  equivalents width are  $14\%$  as they are derived from a ratio of two quantities each with an uncertainty of  $10\%$ . The uncertainties for the reddening and abundances are derived by propagating the errors. The uncertainties of all reddening values are  $0.12$  mag. Propagating the flux errors for the abundances determination (see Sect. 3.8), the uncertainty is just  $0.03$  for the oxygen abundances. Since the scatter of the abundance diagnostics used to derive the oxygen abundance itself is  $0.14$  dex (Pettini & Pagel 2004), this will dominate the overall uncertainty. Similarly, taking into account possible ranges of temperatures to derive the N abundance we find a  $0.2$  dex uncertainty for the N/O ratio. For the oxygen abundance derived in Sect 3.8 we use the solar value  $12+\log(O/H)=8.66$  (Asplund et al. 2004).

Region	[O II] $\lambda 3727$	H $\beta$	[O III] $\lambda 5007$	H $\alpha$	[N II] $\lambda 6584$	[S II] $\lambda 6716$	[S II] $\lambda 6731$	EW(H $\alpha$ ) (Å)	EW(H $\beta$ ) (Å)	<i>B</i> (mag)	<i>V</i> (mag)	<i>R</i> (mag)	<i>E<sub>B-V</sub></i> (mag)	12+log(O/H)	log(N/O)
Galaxy	2400.0	445.0	1293.0	1793.0	197.0	283.0	68.0	67.	13.	15.31	15.08	14.85	0.30	8.27	-1.50
WR reg	694.6	174.0	815.0	603.0	47.9	51.9	39.78	744.	141.	18.64	18.27	18.3	0.17	8.16	-1.50
SN reg	26.07	7.55	18.27	44.94	5.03	9.19	6.84	178.	16.	20.28	20.21	19.8	0.63	8.30	-1.28
WR(-8.7, 0.0)	436.5	142.0	719.0	419.0	30.2	30.5	24.1	1140.	226.	19.16	18.72	18.92	0.03	8.14	-1.42
SN(-5.3, -2.7)	8.11	2.83	7.14	19.42	2.33	4.34	3.17	208.	22.	21.28	21.24	21.17	0.75	8.31	-1.17
-11.4, 11.3	0.80	0.74	0.57	9.41	1.13	1.51	1.13	79.	6.2	20.96	21.12	20.74	1.29	8.47	-0.64
-8.0, 12.0	2.77	1.47	1.20	9.23	1.59	2.43	1.90	75.	12.	21.93	21.20	20.72	0.68	8.51	-0.83
-6.7, 8.0	1.68	1.11	1.40	7.75	0.96	1.36	1.15	38.	5.2	21.04	20.57	20.24	0.78	8.41	-0.88
-4.0, 7.3	6.30	3.43	3.89	16.08	2.01	2.50	1.83	62.	12.	20.59	20.22	19.92	0.43	8.41	-0.98
-2.0, 14.0	6.43	2.01	2.60	11.13	1.57	1.89	1.54	74.	12.	21.28	20.80	20.50	0.57	8.42	-1.16
-1.3, -6.1	3.80	1.70	2.37	17.68	2.05	3.13	2.19	420.	16.	21.47	21.52	21.37	1.12	8.38	-1.00
-1.3, 10.0	2.13	1.45	0.92	7.87	1.15	1.53	1.25	34.	5.6	20.67	20.35	20.06	0.56	8.53	-0.81
-0.7, 1.3	34.1	11.80	25.51	48.51	6.29	5.04	3.61	119.	25.	20.14	19.65	19.38	0.32	8.34	-1.15
-0.0, 3.3	2.19	1.32	3.13	7.56	1.22	1.62	1.22	29.	4.5	20.65	20.21	19.94	0.60	8.36	-0.84
2.0, 12.7	0.00	0.84	0.83	5.25	0.73	1.27	1.08	230.	4.9	21.17	20.76	20.43	0.67	8.46	...
2.7, 1.3	4.34	4.20	3.52	17.25	2.56	2.77	1.83	296.	15.	20.44	20.44	20.26	0.32	8.49	-0.65
2.7, -4.0	6.34	0.92	1.27	10.97	1.59	2.76	1.96	2411.	13.	21.73	21.87	21.82	1.23	8.42	-1.32
5.4, 6.0	2.84	3.04	2.76	13.14	1.91	2.34	1.72	38.	7.3	20.23	19.86	19.62	0.36	8.48	-0.62
6.1, 10.7	5.59	4.57	4.74	16.04	2.44	3.50	2.48	58.	12.	20.25	19.98	19.85	0.18	8.46	-0.70
8.7, 0.6	8.15	6.65	3.40	15.95	2.04	4.53	2.84	49.	17.	20.16	19.90	19.37	0.00	8.54	-0.83
9.4, -3.3	28.3	17.39	37.42	42.96	4.77	7.03	5.20	254.	56.	21.24	21.02	21.07	0.00	8.32	-1.00
10.1, 8.0	0.24	2.70	4.96	10.82	1.33	1.83	1.31	47.	8.2	20.26	20.18	20.19	0.29	8.35	-0.64
11.4, 4.6	21.7	12.18	27.19	27.10	4.52	4.07	3.02	149.	19.	19.63	19.43	18.94	0.00	8.37	-0.92
12.1, 13.3	0.00	0.77	0.76	3.68	0.52	0.70	0.59	38.	4.7	21.27	20.97	20.99	0.45	8.46	...
14.8, 3.3	13.6	3.42	6.00	9.25	1.00	1.92	1.34	61.	15.	20.70	20.55	20.08	0.00	8.34	-1.36
14.8, 10.0	7.49	3.48	4.85	7.28	1.16	1.53	1.39	79.	25.	21.11	21.08	20.98	0.00	8.43	-1.03
mean	29.±94	10.±29	38.±149	33.±85	3.±6	4.±6	3.±5	152.±243	24.±46	20.5±0.6	20.3±0.7	20.0±0.6	0.46±0.40	8.41±0.09	-0.91±0.34

**Table 2.** Fluxes for the strong emission lines in units of  $10^{-16}$  erg s $^{-1}$  cm $^{-2}$  corrected for Galactic extinction. The magnitudes are given in AB units. The first three rows correspond to different aperture sizes. For the WR and SN region the radial apertures are 2'' defined to include all the flux from the regions seen in the H $\alpha$  image. Below the first three rows the fluxes are extracted from the images in a square aperture of  $3 \times 3$  spaxels equivalent to 4 arcsec $^2$  around the coordinates in Column 1. The magnitudes are calculated from the spectra extracted within this aperture. Note that the properties vary with the chosen aperture; especially the equivalent widths show differences as described in Sect. 3.4. The oxygen abundance and N/O abundance ratio in the two last columns are discussed in Sect. 3.8. The uncertainties for line fluxes and magnitudes are  $\approx 10\%$ ,  $< 4\%$  for the H $\alpha$  and H $\beta$  EW, 0.12 mag for the reddening, and 0.14 dex for the oxygen abundance calibration. The uncertainty of the N/O ratio is 0.2 dex. The last row gives the mean of the individual regions, and the uncertainty is the standard deviation.

### 3.3. Kinematics

Even though the lines are not exactly Gaussian in shape, we can use an automated line fitting routine to estimate the position of the peak of the  $H\alpha$  line to derive the velocity structure in the galaxy as presented in Fig. 3. The zero-velocity is defined for the geometric centre of the galaxy. The uncertainty of the wavelength calibration for each spaxel is less than  $0.2 \text{ \AA}$ , which corresponds to a velocity uncertainty of  $10 \text{ km s}^{-1}$ .

To derive the kinematic mass for the whole galaxy, it is necessary to sample the rotation curve in the flat part in the outskirts of the disk. In the velocity map there is a gradient that increases all the way to the edge, so the estimated kinematic mass is limited to within  $15''$  or correspondingly  $2.6 \text{ kpc}$  in radius. We model the rotation of the galaxy assuming a simple rotation of a solid disk. This is appropriate at least for the central part of the galaxy because of the presence of a bar in the centre. The only free parameters are the centre of the disk, the position angle and the velocity. The model velocity field is subtracted from the observations, and the model with the smallest velocity residuals are taken as the best fit. A best fit model of the velocity field within the VIMOS FOV gives a maximum rotation velocity of  $25 \text{ km s}^{-1}$  at this distance. With these values the mass is  $4 \times 10^8 / (\sin i)^2 M_\odot$ , where  $i$  is the inclination of the galaxy. For  $i \approx 50^\circ$  estimated from surface photometry of the high surface brightness emission in the FORS  $B$  band image, the lower limit to the galaxy mass is  $6 \times 10^8 M_\odot$  within the VIMOS FOV. The largest uncertainty comes from the estimate of the inclination, since most of the galaxy does not have a high surface brightness, and could result in an underestimation by a factor of  $\sim 5$ . The total galaxy mass derived from a  $K$  band image ( $1.1 \times 10^9 M_\odot$ ) indicates a stellar mass about twice the value within the VIMOS FOV (Castro Cerón et al. 2008). If the inclination axis is lower than  $50^\circ$ , the ratio of the total mass indicated from the velocity to the stellar mass increases correspondingly, i.e. the dark matter halo mass increases.

The estimated mass is consistent with the mass-luminosity-metallicity relation for SDSS galaxies (Tremonti et al. 2004), which predicts  $12 + \log(\text{O}/\text{H}) = 8.5 \pm 0.2$  for a galaxy with this (stellar) mass. The dynamical mass estimate includes both stellar and dark matter, so counting only the stellar mass implies a lower expected abundance. In Sect 3.8 we find an oxygen abundance of  $12 + \log(\text{O}/\text{H}) = 8.3$ , which is in agreement with a relatively small mass galaxy (See also Table 2).

### 3.4. Equivalent widths

The continuum around the  $H\alpha$  and  $H\beta$  lines was calculated in order to determine the equivalent widths (EWs) corrected for the underlying stellar absorption. The resulting maps are shown in Fig. 4. The WR region clearly stands out in this image. In the WR region the  $H\alpha$  and  $H\beta$  EWs are  $744 \text{ \AA}$  and  $141 \text{ \AA}$  within a  $2 \text{ arcsec}$  radial aperture, while in the SN region the EWs are  $178 \text{ \AA}$  and  $16 \text{ \AA}$ , respectively. The  $H\alpha$  value for the SN region is larger by a factor of two compared that in Hammer et al. (2006), which is likely due to aperture effects for long slit spectra or differences in the size of the extracted regions. The fewer extracted spaxels the larger the EWs. As an example the EW in the brightest spaxel in the WR region has an  $H\alpha$  EW of  $1600 \text{ \AA}$ . According to instantaneous burst models from Starburst99 (Leitherer et al. 1999), this corresponds to an age of  $3.1 \text{ Myr}$ . Similarly, the brightest spaxel of the SN region has an  $H\alpha$  EW of  $320 \text{ \AA}$ , corresponding to an age of  $5.0 \text{ Myr}$ . If we analyse the EWs for the

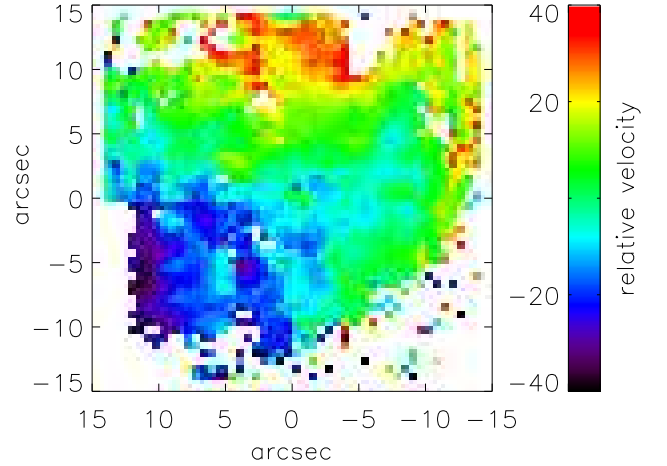


**Fig. 3.** Velocity map derived from fits to the  $H\alpha$  emission line in all spaxels. The values are in units of  $\text{km s}^{-1}$ . See the electronic edition of the Journal for a colour version.

other  $H\text{ II}$  regions in the host, we find that the SN region is more representative for the host galaxy as a whole, while the WR region is the youngest.

### 3.5. Intrinsic reddening

The ratio of the maps  $H\alpha/H\beta$  gives a measure of the reddening by dust. In the Case B recombination scenario, the theoretical dust free ratio is 2.85 for a temperature of  $10\,000 \text{ K}$  (Osterbrock 1989). The reddening is calculated using the equation  $E_{B-V} = 1.98 [\log_{10}(H\alpha_{\text{obs}}/H\beta_{\text{obs}}) - \log_{10}(2.85)]$ . The factor 1.98 assumes a Milky Way type extinction law (Fitzpatrick 1999), but choosing a different extinction curve does not change this factor significantly. The reddening map is presented in Fig. 5. We have adopted a threshold for the  $H\alpha$  flux of  $3 \times 10^{-17} \text{ erg s}^{-1} \text{ cm}^{-2}$  to calculate the extinction, because in regions where the flux is lower, the value of  $E_{B-V}$  gets correspondingly uncertain. Whereas the host has an overall  $E_{B-V} = 0.30 \text{ mag}$ , approximately half of the WR region appears dust free with an overall average of  $0.17 \text{ mag}$ . The SN region, on the other hand, appears to have significantly more reddening: the estimated average  $E_{B-V} = 0.63 \text{ mag}$ . A similar analysis can be done using the  $H\beta/H\delta$  emission line ratio but this ratio has a larger uncertainty due to the fainter emission lines involved. The results obtained from this ratio agree with that of  $H\alpha/H\beta$  within the uncertainties. Using the tight correlation between the  $H\alpha$  and  $24\mu\text{m}$  luminosities (Kennicutt et al. 2007) together with the IR luminosity of  $2.34 \times 10^{40} \text{ erg s}^{-1}$  for the WR region (Le Floc'h et al. 2006), we find an overall 3% extinction correction to the  $H\alpha$  flux. The spatial resolution of Spitzer is not sufficient to separately resolve the SN region.

The reddening inferred from the FORS archive spectrum is  $E_{B-V} = 0.16$  and  $0.14 \text{ mag}$  for the WR and SN region, indicating a large discrepancy only for the SN region. For this region Sollerman et al. (2005) find  $E_{B-V} = 0 \text{ mag}$ , while Hammer et al. (2006) find  $E_{B-V} = 0.39 \text{ mag}$ , and Savaglio et al. (2008) find  $A_V = 1.73$ . If the extinction in the SN region is really as high as what we find, this implies that the supernova was exceptionally (unreasonably) bright and blue. If the extinction is really larger compared to that inferred from the observations of SN 1998bw, this could imply that the SN was in the foreground of a dustier  $H\text{ II}$  region.



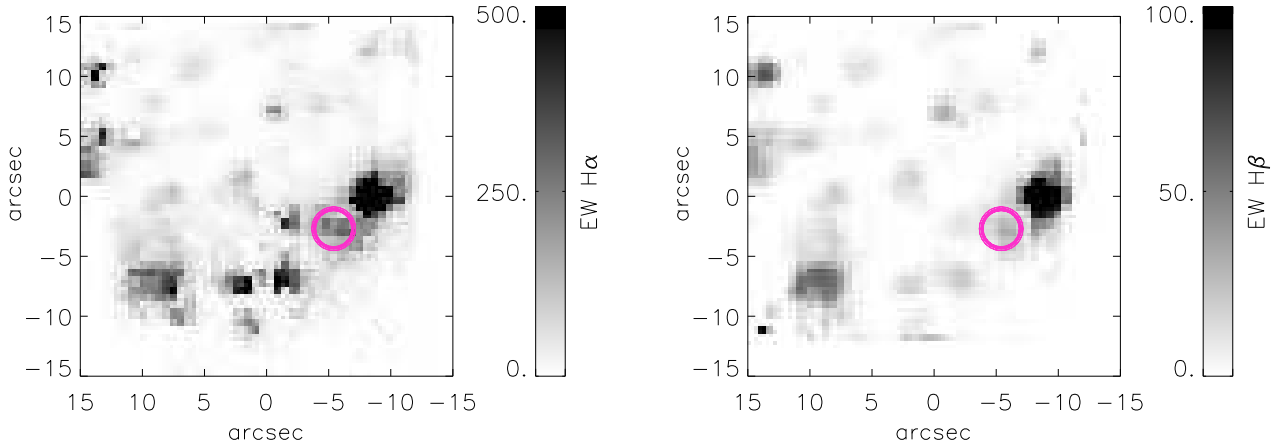


**Fig. 4.** Map of the  $H\alpha$  EW (left panel) and map of the  $H\beta$  EW (right panel). The noise pattern in the lower middle part of the  $H\alpha$  EW map is caused by noise in the continuum flux estimate in the VIMOS data. In this region the surface brightness is low (see Fig. 1). Both panels show that the WR region has the largest EW over the face of the galaxy, and indicating that this is the youngest star forming region. The circle marks the position of the SN.

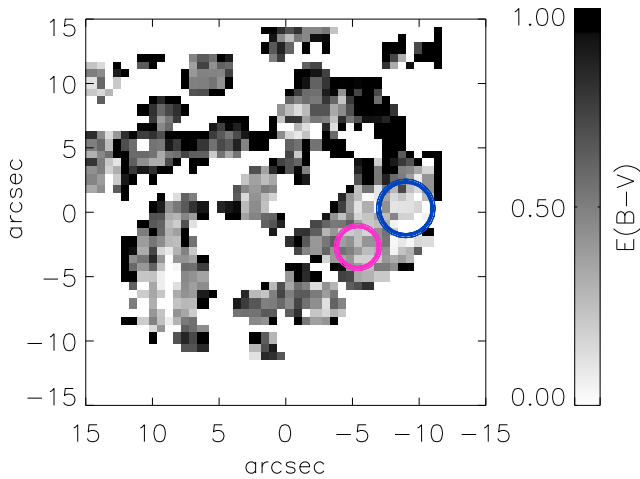


**Fig. 5.** Reddening map, showing the value of  $E_{B-V}$ . Half of the WR region at coordinates  $(-8.7, 0)$  appears relatively free of dust (white colour), while the SN region has  $E_{B-V} = 0.63$  mag. The small circle indicates the location of the SN region, and the larger circle the location of the WR region. Apart from the white colour in the WR region, white regions in this and following maps represent spaxels where the  $H\alpha$  flux is smaller than  $3 \times 10^{-17} \text{ erg s}^{-1} \text{ cm}^{-2}$ .

The magnitudes of the SN region in the FORS images and the VIMOS data are in agreement to within 0.05 mag when the same aperture size is used. Because the long slit data cannot be used to calculate the magnitude as a consistency check, we assume that the large extinction found in the VIMOS data is correct, even though there is a large discrepancy with some literature values.

### 3.6. Star formation rates

The  $H\alpha$  emission line flux can be converted to a SFR given the transformation in Kennicutt (1998). This law has been derived for galaxy disks as a whole, and may not be appropriate for individually resolved  $H II$  regions and for very young regions that experience almost instantaneous bursts of star formation. The

ages derived for individual  $H II$  regions in the GRB 1998bw host are similar, and the  $H\alpha$  luminosities are sufficiently high, so we can assume that the  $H\alpha$  luminosity to SFR conversion is applicable for individual regions (see also Kennicutt et al. 2007). A map of the SFR surface density is shown in Fig. 6.

As derived from the  $H\alpha$  emission line luminosity the total SFR within the FOV is  $0.21 \text{ M}_{\odot} \text{ yr}^{-1}$ . From the integrated one-dimensional spectrum over the whole FOV we find  $\text{SFR} = 0.23 \text{ M}_{\odot} \text{ yr}^{-1}$ . The difference represents the uncertainties for estimating the underlying continuum, which differs in the two cases: From the image, the continuum is estimated in each spaxel, while this is only done in one dimension in the extracted spectrum. Within the 30 arcsec square aperture the  $H\alpha$  narrow-band image presented in Sollerman et al. (2005) gives  $0.22 \text{ M}_{\odot} \text{ yr}^{-1}$  (corrected for 10% flux from  $[N II]$  which falls in the narrow band too).

A sample of GRB host galaxies at  $z \sim 1$  have typical UV based specific star formation rates (SSFRs) around  $10 \text{ M}_{\odot} \text{ yr}^{-1} (L/L^*)^{-1}$ , where the luminosities  $L$  are normalised to the  $B$  band luminosity  $L^*$  corresponding to the magnitude  $M^* = -21$  (Christensen et al. 2004a). To determine the SSFR of the GRB 980425 host, the spectra in the blue high resolution cube are convolved with a Bessell transmission function (Bessell 1990) to get the  $B$  band magnitude in each spaxel. Then the SFR map is divided by the relative luminosity  $L/L^*$  as shown in the right panel in Fig. 6, which essentially measures the  $H\alpha$  flux relative to the blue continuum luminosity. In the WR region the  $H\alpha$  flux is much larger for a given continuum flux than in other regions.

Since the SFR measure is more relevant on a galaxy wide scale we analyse the integrated properties for the galaxy too. The integrated magnitude in the VIMOS data is  $m_B = 15.3$  mag corresponding to an absolute magnitude of  $M_B = -17.5$ , which gives  $\text{SSFR} = 5.3 \text{ M}_{\odot} \text{ yr}^{-1} (L/L^*)^{-1}$ . This is slightly smaller than the UV based SSFRs for higher redshift GRB hosts. The entire GRB host has a  $\text{SSFR} \approx 7 \text{ M}_{\odot} \text{ yr}^{-1} (L/L^*)^{-1}$  (Sollerman et al. 2005). If we apply a correction for the internal extinction in the host ( $E_{B-V} = 0.3$ ) we find  $\text{SSFR} = 10.2 \text{ M}_{\odot} \text{ yr}^{-1} (L/L^*)^{-1}$ .

The very high value for the WR region stands out compared to the sample of GRB hosts at  $z \sim 1$ . However, the explanation is that the individual star forming regions are resolved (here normalised to  $\text{kpc}^{-2}$ ), while the higher redshift hosts are



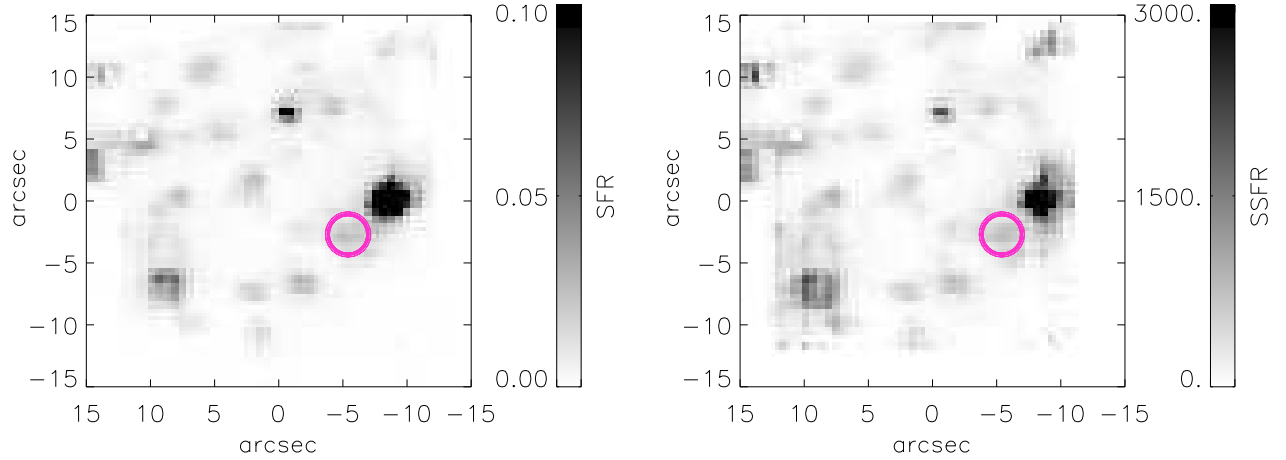


**Fig. 6.** Left panel: Map of the SFR converted from the  $H\alpha$  map. The units are in  $M_{\odot} \text{ yr}^{-1} \text{ kpc}^{-2}$ . Right panel: Map of the luminosity specific SFR in units of  $M_{\odot} \text{ yr}^{-1} (L/L^*)^{-1} \text{ kpc}^{-2}$  (not corrected for intrinsic extinction in the host). The WR region has the largest value over the face of the host. The circle marks the location of the SN region.

investigated using integrated properties. Other lower redshift GRB host with very high SSFRs include the GRB 030329 host with  $\sim 25 M_{\odot} \text{ yr}^{-1} (L/L^*)^{-1}$  (Gorosabel et al. 2005), and the GRB 031203 host with  $\text{SSFR} \sim 39 M_{\odot} \text{ yr}^{-1} (L/L^*)^{-1}$  (Sollerman et al. 2005). All these values are derived from emission line based SFRs, and it is known that there are discrepancies between the SFRs determined from the UV flux and that from emission lines, albeit the discrepancies found are typically a factor less than 2. Nevertheless, the high values for GRB hosts are unusual relative to field galaxies, which typically have UV continuum based  $\text{SSFR} \lesssim 5 M_{\odot} \text{ yr}^{-1} (L/L^*)^{-1}$  (Christensen et al. 2004a).

### 3.7. Electron temperature and densities

Ideally the temperatures and densities of the  $H II$  regions should be derived including faint nebular emission lines such as the  $[O III] \lambda 4363$ , or the  $[N II] \lambda 5755$  line (Osterbrock 1989). Only for one region do we detect the temperature sensitive  $[O III] \lambda 4363$  line (right panel in Fig. 2). In the FORS data we also only detect the faint line in the WR region. From the ratio  $O3 = (4959 + 5007)/4363$  we find  $T = 10\,300 \pm 1000 \text{ K}$  for the WR region. In comparison Hammer et al. (2006) find temperatures for the SN and WR region between 11 000 and 12 000 K.

To determine the electron densities we analyse the ratio of the  $[S II] \lambda \lambda 6717, 6731$  lines using the IRAF package NEBULAR, which is built on the code presented in Shaw & Dufour (1995). At the spectral resolution of VIMOS ( $R \sim 2900$  as measured from sky lines) the sulfur lines are clearly separated, while the lower resolution in the FORS spectrum ( $R = 650$ ) blends the lines. The WR region has a density of  $120 \text{ cm}^{-3}$  derived from the  $[S II]$  line ratio, which for most regions is close to 1.3. Since the flux calibration does not affect the uncertainty of the ratio, the error for the ratio is 0.03 based on the number counts in the spectra. A density of the order  $100 \text{ cm}^{-3}$  is typically derived for other GRB hosts (Prochaska et al. 2004; Wiersema et al. 2007; Savaglio et al. 2008).

### 3.8. Abundances

We use the O3N2 abundance diagnostics from Pettini & Pagel (2004) to determine the oxygen abundance. This diagnostics involve the line flux ratios  $[O III] \lambda 5007/H\beta$  and  $[N II] \lambda 6586/H\alpha$

whose lines are close in wavelength so that extinction plays a minor role. Figure 7 shows the metallicity map of the host galaxy and illustrates the values in Table 2 in the units  $12 + \log(O/H)$ , with the solar value of 8.66 adopted from Asplund et al. (2004). Extracting the one-dimensional spectra of the WR and SN regions yields  $12 + \log(O/H) = 8.16$  and 8.30, respectively, which corresponds to 0.32 and 0.44 solar abundance. The uncertainties of the abundance is 0.03 dex if we propagate the uncertainties of the emission line fluxes. Compared to this, the  $1\sigma$  scatter of 0.14 dex for the data points used to derive the O3N2 diagnostics will dominate (Pettini & Pagel 2004). The calibration is derived for values of  $O3N2 < 1.9$ , which is valid for all the regions in the GRB host. Considering the large scatter of the calibration, the derived metallicities in Table 2 are similar within  $3\sigma$ , and the WR and SN region metallicities are consistent within  $1\sigma$  even.

While the value for the WR region is lower than for other regions, it is also striking that the SN region has the second lowest metallicity, however within the uncertainties many other regions have the same abundance. Since these metal poor regions have brighter emission lines than the remaining regions, they will dominate the total spectrum of the host even though some values in Table 2 imply higher abundances (0.6–0.8 solar). The total galaxy spectrum has  $12 + \log(O/H) = 8.27$  (0.40 solar), i.e. similar to that of the SN region.

Using the N2 abundance diagnostics from Pettini & Pagel (2004) gives the same abundances within the uncertainties, while the S2 diagnostics, that use the  $H\alpha/[S II] \lambda \lambda 6717, 6731$  ratio and the O3N2 calibration in Yin et al. (2007) give systematically larger abundances by 0.1–0.15 dex for all regions. The calibration in Yin et al. (2007) is derived from a larger sample of galaxies than in Pettini & Pagel (2004), where the calibration is derived from  $H II$  regions, for which the abundances are derived from the temperature sensitive lines. It is well known that different diagnostics imply differences in the abundances (Kewley & Ellison 2008), and here we do not attempt to correct for the diagnostics used. The important point for the GRB host is not the absolute values of the metallicity, but the variations of the metallicity over the face of the galaxy, and that one particularly bright region can dominate the integrated abundance.

In the WR region, where the temperature sensitive  $[O III] \lambda 4363$  line is detected with a flux of  $\sim 5 \times 10^{-16} \text{ erg s}^{-1} \text{ cm}^{-2}$ , the equations in Izotov et al. (2006), together

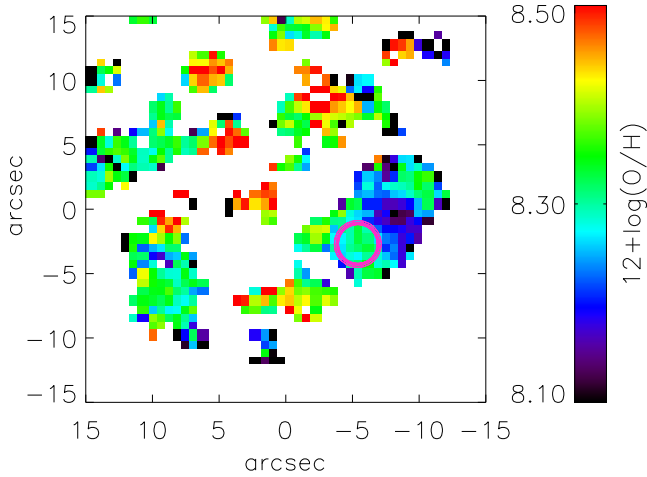


**Fig. 7.** Oxygen abundance map derived from the O3N2 abundance diagnostics. The WR region has the lowest abundance in the whole galaxy, and the SN region has the second lowest abundance although similar to other regions within the  $1\sigma$  uncertainty of 0.14 dex. The circle indicates the location of the SN region. [See the electronic edition of the *Journal* for a colour version of this figure.]

with the de-reddened fluxes lead to an oxygen abundance of  $12+\log(\text{O}/\text{H})=8.53\pm0.10$ , which is significantly larger than that derived from the O3N2 diagnostics. This discrepancy suggests that the O3N2 diagnostics may not be a valid approximation for this particular galaxy, and that the abundance may even be on average close to solar in contradiction to the general idea that GRB progenitors and their hosts have sub solar metallicities.

The strong emission lines in Table 2 can be used to derive the (N/O) abundance ratio. To calculate this ratio we added the contributions to the abundance  $\text{O}/\text{H}^+ = \text{O}^+/\text{H}^+ + \text{O}^{2+}/\text{H}^+$ , and N is obtained by multiplying the  $\text{N}^+/\text{H}^+$  ratio with an ionisation correction factor using the equations in Izotov et al. (2006). The results are presented in the last column in Table 2. For the different H II regions a constant temperature of  $10^4$  K is assumed. This is the strongest assumption which can lead to a ratio which is 0.2 dex lower if the temperature is 2000 K lower. Correspondingly a 0.2 dex higher ratio would require the temperatures to be larger by  $\sim 3000$  K. However, such a high electron temperature is not expected since most regions are not particularly oxygen poor. A low temperature ( $<8000$  K) would imply a N/O ratio which is lower than found for most metal poor galaxies ( $\log(\text{N}/\text{O}) = -1.8$ ). The uncertainties of the line fluxes imply an uncertainty of 0.1 dex. Since the densities for the various regions are close to  $100 \text{ cm}^{-3}$ , the small differences do not imply a significant correction to the N/O ratio. Overall this implies an uncertainty of the N/O ratio of 0.2 dex.

The N/O ratio can be used to probe the star formation history of the galaxy given the different time scale for the primary nitrogen production vs. the secondary contribution of nitrogen from intermediate mass stars. Compared to the solar value of  $\log(\text{N}/\text{O})_{\odot} = -0.81$  (Holweger 2001), most of the regions have sub solar values. Within the uncertainties the WR and SN regions have similar values of N/O, while again the value for the whole galaxy is dominated by these bright H II regions. Taken at face value the N/O ratios indicate that the WR region is the youngest, but not as young as the N/O ratio suggests for some damped Lyman $\alpha$  systems (Centurión et al. 2003; Pettini et al. 2008). Contamination from previous generations of stars to the

gas over time scales larger than 100–300 Myr in the WR region is responsible for this effect. The presence of WR stars is expected to increase the N/O ratio (Meynet & Maeder 2005), however Izotov et al. (2006) find that the enhancement is small. For GRB hosts it still remains unclear whether an enhancement of Nitrogen is present because the measurement errors are large (see Wiersema et al. 2007).

### 3.9. Stellar population modeling

The observed spectra are fit with the spectral templates derived from simple stellar evolution models from Starburst99 (Leitherer et al. 1999), which includes both stellar and nebular emission. We chose to fit the VIMOS spectra with models of 0.4 solar metallicity as this is the most representative value for the host galaxy. The models assume an instantaneous burst of star formation, and a Salpeter law initial mass function between 1 and  $100 M_{\odot}$ . The best fit templates are determined from a standard  $\chi^2$  fitting technique. Using the intrinsic extinction in Table 2 to de-redden the spectra before fitting the models we find that the best fit age of 6 Myr for the WR region, whereas the best fit age is 3 Myr for the SN region due to the large intrinsic extinction. For all H II regions the best fit ages lie between 2 and 10 Myr as listed in Column 4 in Table 3. With the smaller intrinsic reddening inferred from the SN region (Sollerman et al. 2005) found an age of 6 Myr, and a corresponding progenitor mass of  $30\pm5 M_{\odot}$ .

For comparison, we also fit the de-reddened spectra from individual regions to the high resolution spectral templates from Bruzual & Charlot (2003). The models assume a single burst population and a Salpeter law initial mass function and again a 0.4 solar metallicity. We generally found a larger scatter between individual H II region with best fit ages between 1 and 200 Myr. Since these models do not include the nebular emission component, which is dominant for the very young regions, the ages determined from the starburst99 model should represent the regions better.

The ages derived from the individual regions are in broad agreement with those derived from the equivalent widths in Sect 3.4, which indicate ages of 3 to 6 Myr for the individual H II regions, and with emission line ratios in Sect. 4. Discrepancies in the individual age estimates are likely caused by uncertainties in the reddening estimate which affect the spectral fittings, while the EWs are largely unaffected by the reddening. The continuum trace older populations of stars, while the emission lines trace the most recent star forming episode. Since the younger regions will have a larger extinction this could affect the EWs. Irrespectively of this fact, both the EWs and the population fittings indicate young ages for all the regions ( $<10$  Myr).

### 3.10. Mass estimates

The best fit Starburst99 models were used to estimate the masses for the different H II regions. Since the template models are created for stellar populations of  $10^6 M_{\odot}$  a simple scaling to the observed spectrum is required to derive the mass. The WR and SN regions (using the first entries in Table 2) have similar masses:  $0.44\times10^6 M_{\odot}$  and  $0.5\times10^6 M_{\odot}$ , respectively, while the mass of the luminous stars in the galaxy is  $2\times10^7 M_{\odot}$ . Uncertainties for the mass estimate includes both the error for the absolute flux, and the correction for the reddening yielding a total uncertainty of 20%.

In Table 3 the masses are used together with estimates of the SFR to derive additional parameters such as mass-to-light ratios

and specific SFRs using the mass as normalization instead of the luminosity for the various regions. Note that the units in column 7 and 8 are different. We checked the mass estimates for the individual regions by comparing the FORS *R* band magnitudes, extracted within the same aperture as the VIMOS spectra, with the model predictions from the 0.4 solar metallicity Bruzual & Charlot (2003) models. We find a general good agreement with the values listed in Table 3. The derived mass depends strongly on the assumed age for the regions and the extinction applied.

Comparing the mass SSFR with the definition of the luminosity SSFR used in Sect. 3.6 (the two last columns in Table 3), the values agree in general within a factor of a few. The determination of the mass SSFR involves additional uncertainties because of model dependencies for the mass-to-light ratio and age determination. These uncertainties do not influence the luminosity SSFR since this quantity only includes directly observed parameters, and this is therefore an excellent proxy for the more generally used mass SSFR. The SSFRs in the table are higher compared to those derived for higher redshift GRB hosts, which have typical extinction corrected luminosity SSFRs =  $1\text{--}30\text{ M}_\odot\text{ yr}^{-1} (L/L^*)^{-1}$  (Christensen et al. 2004a). The reason is that the extinction determined from the emission line ratios in the H II regions are much larger than found from the integrated spectral energy distributions, so the correction applied to the SFRs are likewise higher.

For the entire galaxy we compared the mass derived from the stellar population model fitting to masses derived from the absolute magnitudes derived from the FORS *R* band image. Within the VIMOS FOV, the relative luminosity is  $L/L_\odot = 10^{9.3}$ . Assuming a mass to light ratio of 0.1 (calibrated using the *K* band as appropriate for GRB hosts as in Savaglio et al. 2008), the mass within the field is  $2 \times 10^8\text{ M}_\odot$ . In comparison the mass estimated from the kinematics is three times larger. We tested this mass estimate with the spectral energy distribution fitting codes Z-Peg (Le Borgne & Rocca-Volmerange 2002), and HyperZ (Bolzonella et al. 2000) on the measured broad band magnitudes. Both SED fitting codes give the same mass to within the uncertainties.

To investigate whether the galaxy is unusual compared to field galaxies, we compared with SFRs measured for SDSS galaxies. The total stellar mass for the host gives an expected star formation rate of  $0.3\text{ M}_\odot\text{ yr}^{-1}$  following the distribution values for galaxies in the SDSS (Brinchmann et al. 2004). The H $\alpha$  flux corrected for the host extinction in Sect. 3.6 is  $0.4\text{ M}_\odot\text{ yr}^{-1}$ , which is within the distribution of SFRs for SDSS galaxies of similar masses. With this SFR and a total mass of  $2 \times 10^8\text{ M}_\odot$  the specific SFR for the host ( $\text{SSFR} = 2.0\text{ M}_\odot\text{ Gyr}^{-1}\text{ M}_\odot^{-1}$ ) lies in the upper end of the distribution for SDSS galaxies (see Fig. 24 in Brinchmann et al. 2004).

### 3.11. Variation of properties in the H II regions

To illustrate the various properties in Table 2 and 3 with respect to the values measured for the SN and WR regions, we calculate for each quantity the difference from the average (here just written for the SFR):

$$\text{Deviation} = \frac{\text{SFR}(\text{SN}) - \langle \text{SFR}(\text{H II}) \rangle}{\sigma(\text{SFR}(\text{H II}))},$$

where  $\langle \text{SFR}(\text{H II}) \rangle$  is the mean value for the SFR, and  $\sigma(\text{SFR}(\text{H II}))$  is the standard deviation as listed in the last row in Table 2 and 3.

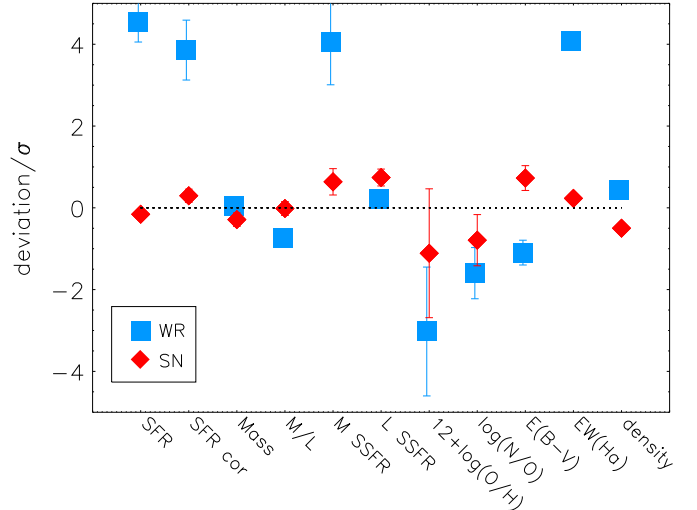


**Fig. 8.** Deviation from the average of the properties listed on the x-axis. The WR region is indicated by squares and the SN region by diamonds. Error bars are in some cases smaller than the symbols.

Figure 8 shows this quantity for all other properties. Notably the SFRs (corrected and uncorrected for the host extinction) of the WR region are significantly ( $4\sigma$ ) above the average for all H II regions, and likewise the abundances are lower for both the WR and SN regions, although the values are actually consistent with the average within the uncertainties. Since the masses of the WR and SN regions are similar, it follows that the extinction corrected mass SSFR is also much higher for the WR region. On the other hand, the luminosity SSFRs for both the SN and WR regions appear to be only slightly above the average. Since the *B* band magnitude of the SN region is much fainter than for the WR region, and no correction for extinction is applied to the magnitude before the luminosity SSFRs are calculated, the luminosity weighted SSFR for the two regions are similar and close to the average for the sample of H II regions. For none of the parameters does the figure change significantly if the median value is used in the calculation instead of the average.

The difference compared to the values in the SSFR map in Fig. 6 is due to the fact that the map is not corrected for internal extinction in the host, whereas the SSFRs in the Tables and in Fig. 8 are extinction corrected.

## 4. Emission line ratios, ages and metallicities

While the SN region in the GRB 980425 host is the second most metal poor region, it is not dust free and most properties (SFRs, EWs, masses) are similar to the remaining H II regions in the host galaxy. In contrast, the WR region seems to be characteristic for what is expected for a GRB region in terms of these properties (see Christensen et al. 2004a).

We compared the emission line ratios  $[\text{O III}]/\text{H}\beta$  vs.  $[\text{N II}]/\text{H}\alpha$  and  $[\text{S II}]/\text{H}\alpha$  to other GRB hosts and other star forming galaxies in Fig. 9. The individual regions (not corrected for the internal extinction in the host) from Table 2 are represented by the small squares. De-reddening the fluxes will not affect the line ratios much. The emission line ratios are compared to those of other GRB host found in the literature. The emission line ratios are usually obtained from integrated spectra of the hosts.

reg.	SFR	SFR (corr.)	Age	Mass	M/L <sub>B</sub>	Mass SSFR (corr.)	Lum SSFR (corr.)
(1)	( $\times 10^{-3} M_{\odot} \text{ yr}^{-1}$ )	( $\times 10^{-3} M_{\odot} \text{ yr}^{-1}$ )	(Myr)	( $\times 10^6 M_{\odot}$ )	( $M_{\odot}/L_{B,\odot}$ )	( $M_{\odot} \text{ Gyr}^{-1} M_{\odot}^{-1}$ )	( $M_{\odot} \text{ yr}^{-1} (L/L_{*})^{-1}$ )
(2)	(3)	(4)	(5)	(6)	(7)	(8)	
Galaxy	233.0	447.0	2	20.1	0.014	22.2	10.9
WR reg.	78.3	113.3	2	0.44	0.007	257.	58.2
SN reg.	5.84	22.9	3	0.50	0.035	45.8	54.3
WR	54.5	58.0	6	0.28	0.007	207.	48.9
SN	2.52	12.9	3	0.20	0.035	64.3	76.4
	1.22	20.1	3	1.15	0.149	17.5	89.1
	1.20	5.25	3	0.18	0.057	29.2	56.8
	1.01	5.48	3	0.43	0.060	12.7	26.1
	2.09	5.32	4	0.22	0.020	24.2	16.7
	1.45	4.99	4	0.19	0.033	26.2	29.6
	2.30	26.1	3	0.46	0.096	56.8	185.1
	1.02	3.45	3	0.28	0.028	12.3	11.7
	6.31	12.6	6	0.20	0.012	63.2	26.3
	0.98	3.61	3	0.35	0.034	10.3	12.0
	0.68	2.92	3	0.26	0.041	11.2	15.7
	2.24	4.49	3	0.13	0.010	34.5	12.3
	1.43	20.6	3	0.46	0.122	44.8	185.3
	1.71	3.73	10	0.57	0.038	6.55	8.43
	2.09	3.08	10	0.29	0.020	10.6	7.09
	2.07	2.07	3	0.08	0.005	25.9	4.39
	5.58	5.58	2	0.07	0.012	79.8	32.0
	1.41	2.64	6	0.10	0.007	26.4	6.13
	3.52	3.52	3	0.12	0.005	29.4	4.58
	0.48	1.27	3	0.11	0.017	11.6	7.48
	1.20	1.20	3	0.04	0.004	30.1	4.19
	0.95	0.95	3	0.03	0.004	31.5	4.80
mean	4.±11	9.±13	4±2	0.3±0.2	0.04±0.04	38.±42	38.±52

**Table 3.** Table for derived quantities for the different regions. The last row gives the mean and standard deviation for all the regions. Column 2 is the SFR derived from the observed H $\alpha$  flux, and col. 3 corrects the SFR for the extinction given in the Table 2. Column 4 gives the best fit age. The mass (col. 5) is determined from population modeling. The mass to light ratio (Col. 6) uses the luminosity  $L_B$  derived from the B magnitude relative to the AB magnitude for the sun  $M_{B,\odot}=5.33$ . Column 7 lists the specific SFR per Gyr normalised to the mass after correction for the host extinction, and Col. 8 lists the luminosity specific SFR, both derived after correcting for intrinsic extinction.

Figure 9 also includes the theoretical emission line ratios for models of H II region of various metallicities and ages (Dopita et al. 2006). Instead of the frequently used ionization parameter, the models involve a parameter,  $R$ , which represents the fraction of the star cluster mass and the pressure in the interstellar medium. For typical stellar masses of the H II regions between  $10^5$ – $10^6 M_{\odot}$  in Table 3, and a temperature of  $10^4$  K and a density of  $100 \text{ cm}^{-3}$  in Sect. 3.7, this implies that  $-1 < \log R < 0$ . The tracks in Fig. 9 assume the fraction  $R = 0$ . For different choices of  $R$  the model ages of the H II regions differ slightly (for details see Dopita et al. 2006), but this will not change the conclusion for the relative ages of the GRB host emission line regions.

Except for GRB 060505 and GRB 060614, all GRB hosts are located at or above the 0.1 Myr model, with their model metallicities between 0.4 and 1 solar. The offset between the models and the data points in the right hand panel which use the  $[\text{S II}]/\text{H}\alpha$  ratio is real, and likely a deficiency of the models because they do not include emission from a diffuse radiation field which would increase the  $[\text{S II}]$  flux. Furthermore, the models of different metallicities for  $[\text{S II}]$  lie very close to each other, whereas they are distinctly separated in the  $[\text{N II}]$  panel. Hence the  $[\text{N II}]/\text{H}\alpha$  line ratio is a better tool to discriminate between metallicities compared to the  $[\text{S II}]/\text{H}\alpha$  line ratio. This may explain why the H II regions are clearly separate from the SDSS galaxies in the left panel, because they are more metal poor than

the SDSS galaxies, while they coincide in the right hand panel. The important point is that in this plot the GRB regions are offset towards the top (smaller age) but still with a range of metallicities. Figure 10 presents a similar plot for the line ratios:  $[\text{O III}]/\text{H}\beta$  vs.  $[\text{N II}]/[\text{O II}]$  and  $[\text{O III}]/[\text{O II}]$ . Note that due to the relatively larger uncertainties for the  $[\text{O II}]$  line fluxes the scatter is larger, but the same trends as in Fig. 9 are seen.

It is interesting to note that in both panels of Fig. 9 and Fig. 10 the WR region lies among most of the other GRB hosts, which are significantly offset towards the top. Similarly the SN region is located to the top relative to the other H II regions in the host. This would indicate that GRBs occur in significantly younger regions – at least in the low redshift hosts where the emission line ratios can be studied.

The GRB 060505 host is also studied through resolved spectroscopy as probed by long slit observations (Thöne et al. 2008). The symbols in Figs. 9,10 correspond to the emission line ratios for the region where the GRB occurred. Emission lines from four other regions are analysed, and although we do not show the individual regions for this host here, the GRB region is also offset to the top relative to the other regions. This implies that in the GRB 060505 host the GRB occurred in the youngest region probed by the long slit spectrum.

We also compare the emission line ratios with the integrated ones for field galaxies in the SDSS. The gray scale background



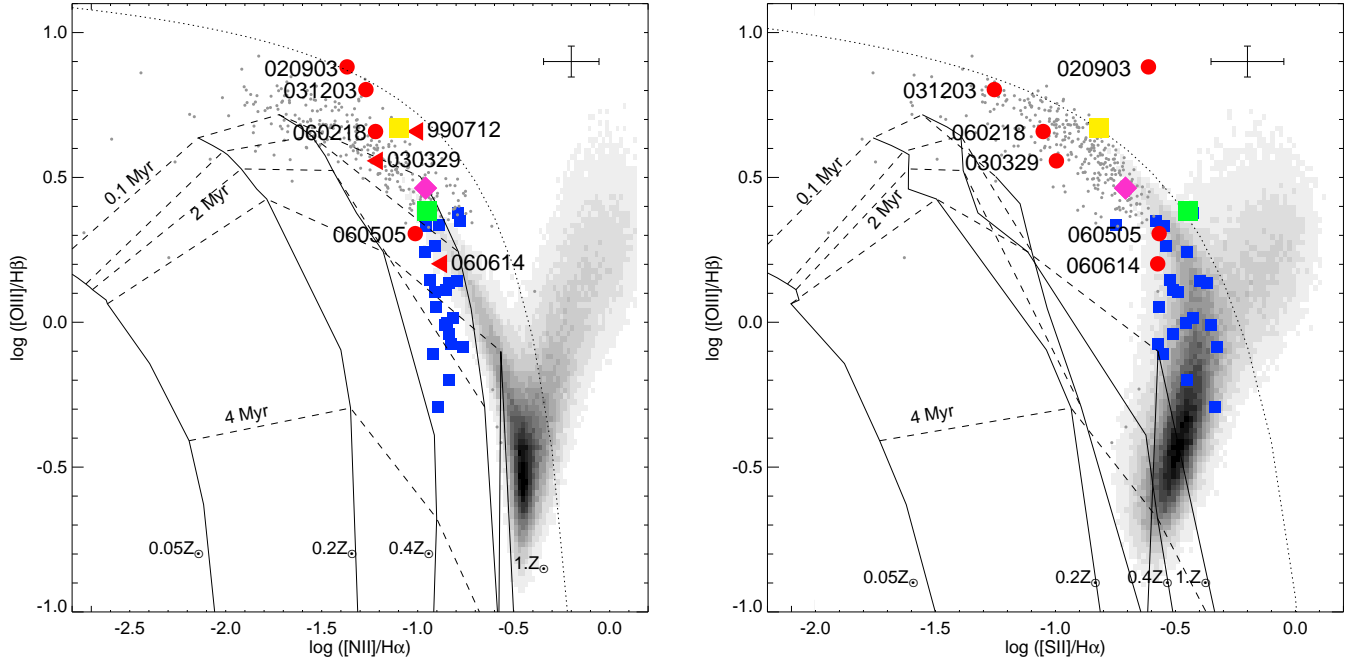


**Fig. 9.** Emission line ratios for GRB hosts:  $[\text{O III}]/\text{H}\beta$  vs.  $[\text{N II}]/\text{H}\alpha$  (on the left) and vs.  $[\text{S II}]/\text{H}\alpha$  (on the right). Individually resolved  $\text{H II}$  regions are shown as small blue squares, the SN region (larger green square), and the WR region (large yellow square), and the entire galaxy (pink diamond). The median error bar for the sample is indicated in the upper right corner. The distinct location of the WR and SN regions indicate that they are special relative to other  $\text{H II}$  regions. The evolutionary models that link emission line regions at ages from 0.1 to 5 Myr for 0.05, 0.2, 0.4 and solar metallicities are taken from Dopita et al. (2006). The dotted, curved lines denote the separation of pure star forming galaxies to AGN dominated emission line ratios (Kewley et al. 2001; Kauffmann et al. 2003). To compare with field galaxies, the gray scale area represent SDSS galaxies (Tremonti et al. 2004), and the small grey dots SDSS galaxies with metallicities between 0.03 and 0.7 solar (Izotov et al. 2006). Emission line ratios for other GRB hosts are overlayed by the named red circles. Two hosts have upper detection limits for  $[\text{N II}]$  and are represented by red triangles (right hand limits); GRB 030329 (Gorosabel et al. 2005) and GRB 990712 (Christensen et al. 2004b). Other references: GRB990712: Küpcü Yoldaş et al. (2006), GRB 031203: Prochaska et al. (2004), GRB 020903: Hammer et al. (2006), GRB 060218: Wiersema et al. (2007), GRB 060614: Gal-Yam et al. (2006), GRB 060505: Thöne et al. (2008). A database is available at the GHostS web site ([www.grbhosts.org](http://www.grbhosts.org)). See the electronic edition of the Journal for a colour version of this figure.

images represent more than 500 000 galaxies in the SDSS DR4<sup>4</sup> (Tremonti et al. 2004). SDSS galaxies that have signatures from WR stars span the full range of emission line ratios measured for other SDSS galaxies (Brinchmann et al. 2008). Clearly not all WR regions in field galaxies are potential progenitor regions for GRBs. Most of these SDSS galaxies are relatively bright, massive, and hence metal rich, so a better comparison might come from a metal poor sample of galaxies. In Figs. 9 and 10 the small individual dots represent galaxies with metallicities between 0.03 and 0.7 solar from the SDSS (Izotov et al. 2006). The selection criteria for the various samples are completely different: the SDSS galaxies are a flux limited sample, the metal poor galaxies are a small sub-sample of the SDSS galaxies with a clear detection of the  $[\text{O III}] \lambda 4363$  line, while the GRB hosts are not affected by these selection criteria. The GRB hosts occupy the similar regions as the metal poor SDSS galaxies, but compared to the models they do not occupy the very metal poor region in the plots.

Most of the individual  $\text{H II}$  regions in the GRB 980425 host occupy a slightly sub solar metallicity region compared to the SDSS galaxies. The scatter of the positions is real and reflects both the age and metallicity spread from one region to the next. As determined in Sect. 3.8, the host galaxy has an oxygen abun-

dance of 0.3–0.8 solar, which is consistent with the model curves in the left panel, where the small squares occupy the model space between these two metallicities.

We can compare these model ages for the individual regions in the GRB 980425 host with those determined from the  $\text{H}\alpha$  and  $\text{H}\beta$  EW measurements in Sect. 3.4. The WR region has an age of 3 Myr according to the EW, while younger ages are suggested by the models in Fig. 9. This is surprising since a very young region ( $< 1$  Myr) is expected to have a high intrinsic extinction, however the IR emission seen in the Spitzer images (Le Floch et al. 2006) does not indicate an optically hidden population of young stars that is not inferred from the  $\text{H}\alpha$  emission. The observations of WR features imply that stellar populations with ages around 3 Myr must be present. The SN region and the integrated spectrum of the galaxy lie between the 1 and 2 Myr evolutionary model line in the plot, i.e. similar to the ages determined from the population model fits, and comparable to the ages derived from the EWs.

## 5. Discussion and conclusions

### 5.1. Implication for high- $z$ GRB hosts

In this paper we have studied the properties of resolved regions in the very nearby host galaxy of GRB 980425/SN 1998bw. We

<sup>4</sup> <http://www.mpa-garching.mpg.de/SDSS/>

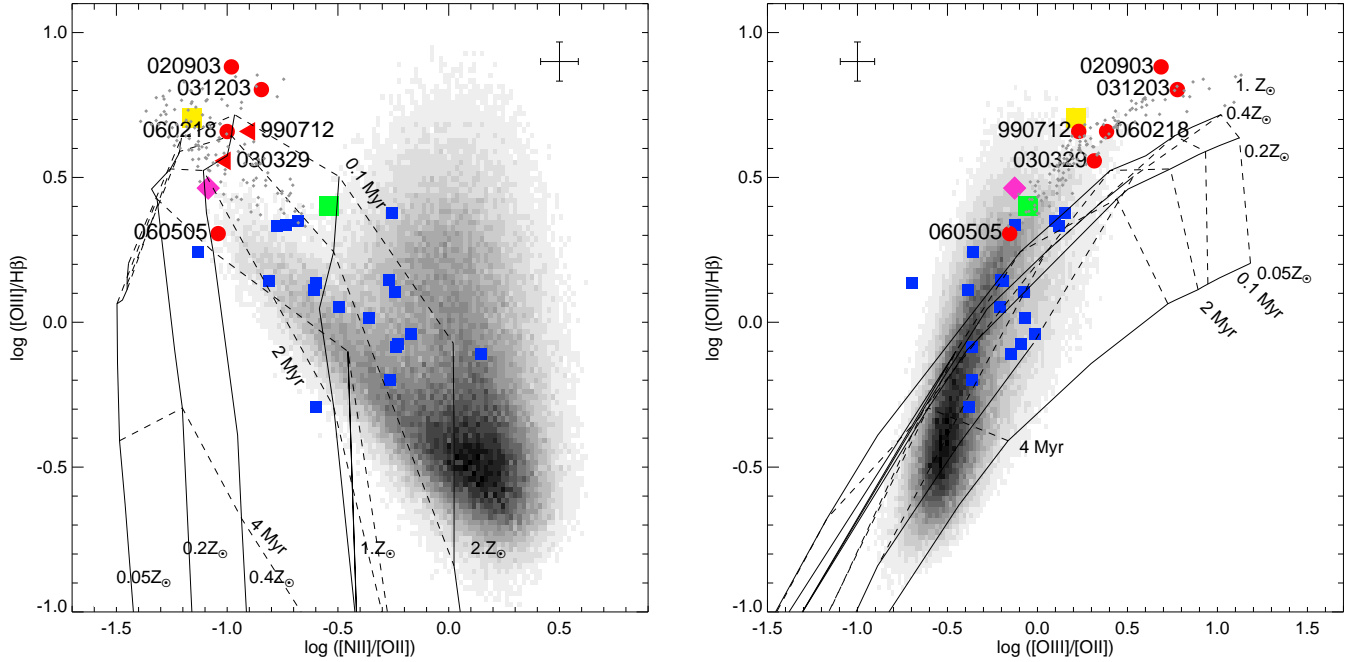


**Fig. 10.** Emission line ratios  $[O\text{ III}]/H\beta$  vs.  $[N\text{ II}]/[O\text{ II}]$  (on the left) and vs.  $[O\text{ III}]/[O\text{ II}]$  (on the right). The symbol shapes and colours are the same as in Fig. 9.

find that the  $H\text{ II}$  region where the GRB/SN occurred has the second lowest oxygen abundance, while the lowest value arises in the WR region. Apart from the metallicity, other physical properties in the SN region are representative for the integrated spectrum of the host galaxy.

The variations, especially those of the metallicity and extinction, over the face of the galaxy have important implications for the interpretations of the observations of higher redshift GRB hosts. In the case that  $z > 1$  GRB hosts do not contain just one (giant) star forming region or star cluster, some properties will not be recoverable when the only information available is the integrated properties of the entire galaxy. In several GRB hosts, the environment appears complex with a few or several individual star forming regions that can only be resolved at the spatial resolution of the HST (e.g. Hjorth et al. 2002).

Based on the study of the resolved population of the GRB 980425 host, we identify the following effects which would occur had the host been at higher redshift and unresolved

- The integrated spectra will decrease the emission line equivalent widths of individual regions, because older stellar populations will be covered. This will substantially decrease the inferred age of unresolved star burst regions.
- The specific star formation rates are much higher in individual  $H\text{ II}$  regions than the integrated one where less active regions are also covered.
- For the GRB 1998bw host galaxy the scatter in oxygen abundances between different regions is relatively small compared to the overall uncertainty of the calibrations. Abundances are similar within  $3\sigma$  uncertainties. In the view of high redshift GRB hosts, the integrated spectra may give a fairly good representation of the abundances in the GRB regions.

- We find that the luminosity SSFR as introduced in Christensen et al. (2004a) for GRB hosts is a good proxy for the mass SSFR which is more frequently used in the literature. Furthermore, the integrated SSFR of the GRB 980425 host is similar to other GRB hosts.
- The extinction for small isolated regions can be severely underestimated. Whereas the overall host has a low reddening of  $E_{B-V}=0.3$  mag, which is normal for (unresolved) higher redshift GRB hosts. The SN region itself has a higher than average value. Relative to spectral energy distribution fitting of GRB host broad band data, the emission line ratios indicate a higher extinction.
- The emission line ratios for the different regions in the host indicate that most other GRB hosts (at  $z < 0.2$ ) have properties that would seem similar to the WR region in the GRB 980425 host. This implies that even though we cannot resolve spatially some GRB hosts, they must be dominated by very young stars, even though we can not always distinguish any WR features in their spectra.
- The separation of 800 pc between the WR and SN region corresponds at  $z = 1$  to a single pixel with the HST spatial resolution of  $0''.1$ . Had the host been at  $z = 1$ , we would be able to resolve only two distinct regions: the centre of the galaxy and the WR region. In a broad band HST image, the GRB location would coincide with the brightest pixel as seen for many cosmological GRBs (Fruchter et al. 2006).

## 5.2. GRB host metallicities

If low metallicities are a necessary prerequisite to create GRBs, this effect should be immediately apparent from the properties of the host galaxies. Theoretical models suggest that GRBs

trace star forming galaxies with less than 10% solar metallicity (Yoon et al. 2006). Models for winds from WR stars are based on Fe as drivers (Vink & de Koter 2005), and likewise the GRB progenitor models are based on the Fe abundance (Yoon & Langer 2005) where no GRB progenitors are expected from stars with metallicities larger than 0.1–0.3 solar (Woosley & Heger 2006; Langer & Norman 2006). However, while the models are based on the Fe metallicity, the emission lines from the host galaxies trace the oxygen abundance.

As demonstrated in Fig. 9 and 10, regions with higher metallicities than the model predictions are generally found among GRB hosts, although these are still below the solar value (see also Savaglio et al. 2008). A potential bias comes from the fact that the hosts are generally very faint, so the metallicity determination has to rely on strong emission line diagnostics, which have large uncertainties. The use of strong emission lines to derive abundances can in some cases give a higher metallicity estimate relative to the direct measurement from the [O III]  $\lambda 4363$  or the [N II]  $\lambda 5755$  emission lines. In the WR region, the strong line diagnostics gives a 0.4 solar oxygen abundance, while the direct measurement indicates a near solar value. As another opposite example the O3N2 diagnostics for the GRB 060218 host indicates a 30% solar oxygen abundance, while the direct method gives just 8% solar (Wiersema et al. 2007).

GRB hosts at  $z > 2$  have generally metallicities around 10% solar as estimated from absorption lines in the afterglows (Savaglio 2006). However, as shown in Vreeswijk et al. (2007) for the case of GRB 060418, the rest frame UV absorption lines do not arise in the immediate GRB progenitor environment, but instead the interstellar medium of the host galaxy along one single line of sight. On the other hand, as we have discussed in this paper, the GRB hosts at low redshift are not necessarily very metal poor. The question is how to relate the low and high redshift sample of GRB hosts to each other when the observing techniques are completely different. Different biases are included from the assumption that the metallicity of the progenitor can be constrained from absorption lines in the GRB afterglow, and that emission lines from the host galaxy can infer the abundance at the progenitor site. Any of these metallicities may not be representative for the GRB progenitor itself. To understand how these two methods compare to each other it is necessary to detect the emission lines and derive abundances from GRB hosts at  $z > 2$  in a similar way as done routinely for local galaxies, and as shown in this paper. By comparing the absorption metallicity, determined from the GRB afterglow, with abundances derived from emission lines it can be verified if the metallicity is representative for the host as a whole, and to place the GRB hosts in relation to star forming field galaxies at high and low redshifts. The comparison of absorption lines and emission line spectroscopy for a high redshift GRB host galaxy can yield the Fe/O ratio. Since the GRB hosts are young and show intense SSFRs it is likely that the oxygen abundance is higher than that derived from Fe due to the relatively smaller contribution from SN Type Ia. Hence, the determination of the Fe/O ratio can provide constraints on the star formation history in galaxies fainter than those generally studied in flux limited surveys.

**Acknowledgements.** LC acknowledges the hospitality of the people at the Dark Cosmology Center in Copenhagen, where much of the data analysis was done. The Dark Cosmology Centre is funded by the Danish National Research Foundation. PMV acknowledges the support of the EU under a Marie Curie Intra-European Fellowship, contract MEIF-CT-2006-041363. JS is a Royal Swedish Academy of Sciences Research Fellow supported by a grant from the Knut and Alice Wallenberg Foundation. Support for ELF's work was provided by NASA through the Spitzer Space Telescope Fellowship Program. We thank Göran Östlin for the H $\alpha$  data check, Sandra Savaglio for useful suggestions

and discussions, and Damien Le Borgne for sharing the Z-Peg code, and finally Avishay Gal-Yam for sharing the Gemini spectrum of the GRB 060614 host. We thank the referee for a constructive report.

## References

- Asplund, M., Grevesse, N., Sauval, A. J., Allende Prieto, C., & Kiselman, D. 2004, *A&A*, 417, 751
- Becker, T. 2002, PhD thesis, Astrophysikalisches Institut Potsdam, Germany
- Bessell, M. S. 1990, *PASP*, 102, 1181
- Bloom, J. S., Kulkarni, S. R., & Djorgovski, S. G. 2002, *AJ*, 123, 1111
- Bolzonella, M., Miralles, J.-M., & Pelló, R. 2000, *A&A*, 363, 476
- Brinchmann, J., Charlot, S., White, S. D. M., et al. 2004, *MNRAS*, 351, 1151
- Brinchmann, J., Kunth, D., & Durret, F. 2008, *A&A*, 485, 657
- Bruzual, A. G. & Charlot, S. 2003, *MNRAS*, 344, 1000
- Castro Cerón, J. M., Michalowski, M. J., Hjorth, J., et al. 2008, *ArXiv e-prints* (astro-ph/0803.2235)
- Centurión, M., Molaro, P., Vladilo, G., et al. 2003, *A&A*, 403, 55
- Chen, H.-W., Prochaska, J. X., Bloom, J. S., & Thompson, I. B. 2005, *ApJ*, 634, L25
- Chen, H.-W., Prochaska, J. X., Ramirez-Ruiz, E., et al. 2007, *ApJ*, 663, 420
- Christensen, L., Hjorth, J., & Gorosabel, J. 2004a, *A&A*, 425, 913
- Christensen, L., Hjorth, J., Gorosabel, J., et al. 2004b, *A&A*, 413, 121
- Dessauges-Zavadsky, M., Chen, H.-W., Prochaska, J. X., Bloom, J. S., & Barth, A. J. 2006, *ApJ*, 648, L89
- Dopita, M. A., Fischera, J., Sutherland, R. S., et al. 2006, *ApJS*, 167, 177
- Filippenko, A. V. 1982, *PASP*, 94, 715
- Fitzpatrick, E. L. 1999, *PASP*, 111, 63
- Fruchter, A. S., Levan, A. J., Strolger, L., et al. 2006, *Nature*, 441, 463
- Fynbo, J. P. U., Holland, S., Andersen, M. I., et al. 2000, *ApJL*, 542, L89
- Gal-Yam, A., Fox, D. B., Price, P. A., et al. 2006, *Nature*, 444, 1053
- Galama, T. J., Vreeswijk, P. M., van Paradijs, J., et al. 1998, *Nature*, 395, 670
- Gehrels, N., Chincarini, G., Giommi, P., et al. 2004, *ApJ*, 611, 1005
- González Delgado, R. M., Leitherer, C., & Heckman, T. M. 1999, *ApJS*, 125, 489
- Gorosabel, J., Pérez-Ramírez, D., Sollerman, J., et al. 2005, *A&A*, 444, 711
- Hammer, F., Flores, H., Schaerer, D., et al. 2006, *A&A*, 454, 103
- Hjorth, J., Sollerman, J., Møller, P., et al. 2003, *Nature*, 423, 847
- Hjorth, J., Thomsen, B., Nielsen, S. R., et al. 2002, *ApJ*, 576, 113
- Holweber, H. 2001, in *American Institute of Physics Conference Series*, Vol. 598, Joint SOHO/ACE workshop "Solar and Galactic Composition", ed. R. F. Wimmer-Schweingruber, 23
- Izotov, Y. I., Stasińska, G., Meynet, G., Guseva, N. G., & Thuan, T. X. 2006, *A&A*, 448, 955
- Jakobsson, P., Levan, A., Fynbo, J. P. U., et al. 2006, *A&A*, 447, 897
- Kaneko, Y., Ramirez-Ruiz, E., Granot, J., et al. 2007, *ApJ*, 654, 385
- Kauffmann, G., Heckman, T. M., Tremonti, C., et al. 2003, *MNRAS*, 346, 1055
- Kennicutt, R. C. 1998, *ARA&A*, 36, 189
- Kennicutt, Jr., R. C., Calzetti, D., Walter, F., et al. 2007, *ApJ*, 671, 333
- Kewley, L. J., Dopita, M. A., Sutherland, R. S., Heisler, C. A., & Trevena, J. 2001, *ApJ*, 556, 121
- Kewley, L. J. & Ellison, S. L. 2008, *ApJ*, 681, 1183
- Küpcü Yoldaş, A., Greiner, J., & Perna, R. 2006, *A&A*, 457, 115
- Langer, N. & Norman, C. A. 2006, *ApJ*, 638, L63
- Le Borgne, D. & Rocca-Volmerange, B. 2002, *A&A*, 386, 446
- Le Floc'h, E., Charmandaris, V., Forrest, W. J., et al. 2006, *ApJ*, 642, 636
- Le Floc'h, E., Duc, P.-A., Mirabel, I. F., et al. 2003, *A&A*, 400, 499
- Leitherer, C., Schaerer, D., Goldader, J. D., et al. 1999, *ApJS*, 123, 3
- Malesani, D., Tagliaferri, G., Chincarini, G., et al. 2004, *ApJ*, 609, L5
- Margutti, R., Chincarini, G., Covino, S., et al. 2007, *A&A*, 474, 815
- Meynet, G. & Maeder, A. 2005, *A&A*, 429, 581
- Modjaz, M., Kewley, L., Kirshner, R. P., et al. 2008, *AJ*, 135, 1136
- Monreal-Ibero, A., Roth, M. M., Schönberner, D., Steffen, M., & Böhm, P. 2006, *New Astronomy Review*, 50, 426
- Osterbrock, D. E. 1989, *Astrophysics of gaseous nebulae and active galactic nuclei* (University Science Books, 1989, 422 p.)
- Pettini, M. & Pagel, B. E. J. 2004, *MNRAS*, 348, L59
- Pettini, M., Zych, B. J., Steidel, C. C., & Chaffee, F. H. 2008, *MNRAS*, 385, 2011
- Prochaska, J. X., Bloom, J. S., Chen, H.-W., et al. 2004, *ApJ*, 611, 200
- Prochaska, J. X., Chen, H.-W., & Bloom, J. S. 2006, *ApJ*, 648, 95
- Prochaska, J. X., Chen, H.-W., Dessauges-Zavadsky, M., & Bloom, J. S. 2007, *ApJ*, 666, 267
- Savaglio, S. 2006, *New Journal of Physics*, 8, 195
- Savaglio, S., Fall, S. M., & Fiore, F. 2003, *ApJ*, 585, 638
- Savaglio, S., Glazebrook, K., & Le Borgne, D. 2008, *ArXiv e-prints* (astro-ph/0803.2718)



- Schlegel, D. J., Finkbeiner, D. P., & Davis, M. 1998, *ApJ*, 500, 525
- Shaw, R. A. & Dufour, R. J. 1995, *PASP*, 107, 896
- Sollerman, J., Holland, S. T., Challis, P., et al. 2002, *A&A*, 386, 944
- Sollerman, J., Östlin, G., Fynbo, J. P. U., et al. 2005, *New Astronomy*, 11, 103
- Stanek, K. Z., Matheson, T., Garnavich, P. M., et al. 2003, *ApJ*, 591, L17
- Starling, R. L. C., Wijers, R. A. M. J., Hughes, M. A., et al. 2005, *MNRAS*, 360, 305
- Thöne, C. C., Fynbo, J. P. U., Östlin, G., et al. 2008, *ApJ*, 676, 1151
- Tremonti, C. A., Heckman, T. M., Kauffmann, G., et al. 2004, *ApJ*, 613, 898
- Vink, J. S. & de Koter, A. 2005, *A&A*, 442, 587
- Vreeswijk, P. M., Ellison, S. L., Ledoux, C., et al. 2004, *A&A*, 419, 927
- Vreeswijk, P. M., Ledoux, C., Smette, A., et al. 2007, *A&A*, 468, 83
- Wiersema, K., Savaglio, S., Vreeswijk, P. M., et al. 2007, *A&A*, 464, 529
- Woosley, S. E. 1993, *ApJ*, 405, 273
- Woosley, S. E. & Heger, A. 2006, *ApJ*, 637, 914
- Yin, S. Y., Liang, Y. C., Hammer, F., et al. 2007, *A&A*, 462, 535
- Yoon, S.-C. & Langer, N. 2005, *A&A*, 443, 643
- Yoon, S.-C., Langer, N., & Norman, C. 2006, *A&A*, 460, 199